High Power Laser Science and Engineering, (2022), Vol. 10, e18, 9 pages.
doi:10.1017/hpl.2022.9

HIGH POWER LASER SCIENCE AND ENGINEERING

RESEARCH ARTICLE

Ultra-compact post-compressor on-shot wavefront measurement for beam correction at PHELIX

J. B. Ohland[1,2], U. Eisenbarth[1], B. Zielbauer[1], Y. Zobus[1,3], D. Posor[1,2], J. Hornung[1], D. Reemts[1], and V. Bagnoud[1,2,4]

[1] *GSI Helmholtzzentrum für Schwerionenforschung, 64291 Darmstadt, Germany*

[2] *Institute for Applied Physics, Technische Universität Darmstadt, 64289 Darmstadt, Germany*

[3] *Institute of Nuclear Physics, Technische Universität Darmstadt, 64289 Darmstadt, Germany*

[4] *Helmholtz-Institut Jena, 07743 Jena, Germany*

(Received 28 January 2022; revised 16 March 2022; accepted 18 April 2022)

Abstract

In order to reach the highest intensities, modern laser systems use adaptive optics to control their beam quality. Ideally, the focal spot is optimized after the compression stage of the system in order to avoid spatio-temporal couplings. This also requires a wavefront sensor after the compressor, which should be able to measure the wavefront on-shot. At PHELIX, we have developed an ultra-compact post-compressor beam diagnostic due to strict space constraints, measuring the wavefront over the full aperture of 28 cm. This system features all-reflective imaging beam transport and a high dynamic range in order to measure the wavefront in alignment mode as well as on shot.

Keywords: adaptive optics; beam quality; high intensity; laser diagnostics; on shot; Strehl; wavefront

1. Introduction

Modern high-intensity lasers are built of several stages of amplification, in which the laser beam dimension is scaled up to several tens of centimeters[1]. These large apertures increase the sensitivity to beam distortions, limiting the intensities and the usage for applications that require near diffraction-limited conditions[2].

Therefore, laser facilities take a large variety of measures to control the spatial and temporal properties of the beam and ensure the highest possible intensities on target. Of these, adaptive optics (AO) is one of the most widely employed techniques, controlling the wavefront (WF) of the beam and thus optimizing the focal spot[3–6].

A typical AO system consists of an optical element that is capable of changing the optical path across the near field (NF) of the beam, often a deformable mirror (DM), followed by an optical system that images the active surface onto a WF sensor to enable closed-loop operation.

Ideally, the WF control in lasers using chirped pulse amplification is split into an AO loop that optimizes the WF going into the compressor (pre-compressor loop) in order to avoid spatio-temporal couplings and another AO loop that optimizes the focal spot after compression (post-compressor loop)[7]. The latter requires a WF sensor that monitors the beam as close to the target as possible, with the goal to deliver a high-fidelity estimate of the on-target intensity. To this end, the concept of equivalent-target-plane imaging coupled to benchmarking diagnostics in the target chamber is one of the most widely accepted strategies[8].

However, this comes with a set of challenges for short-pulse high-energy laser systems, as the compressed pulse features a much higher intensity. On one hand, this prevents using conventional refractive optics for imaging within the main beam path due to non-linear effects in the optical medium and low damage thresholds. However, even for sampled beams with reduced energies, dispersion and chromatism of these optics degrade the imaging quality. On the other hand, as large-aperture refractive optics with small F-numbers are difficult to manufacture due to the need for aspherical surfaces, the scale of these imaging systems is constrained.

As a result of these challenges, refraction-based imaging systems for post-compressor beam diagnostics require a large footprint with lengths often exceeding 10 m[9–13] and, for broadband pulses, measures to compensate for any

Correspondence to: J. B. Ohland, GSI Helmholtzzentrum für Schwerionenforschung, Planckstraße 1, 64291 Darmstadt, Germany. Email: j.b.ohland@gsi.de

induced chromatism have to be taken, for example custom large-aperture achromatic lenses[14], Fresnel lenses[15], Offner imaging systems combined with concave lenses[16] and many more.

The obvious solution for these issues is to use reflective optics to image the surface of the phase modulation component, for example, a DM, to the WF sensor. Corresponding implementations using a number of spherical mirrors do exist or are planned[10,14,17]. While this solves the chromatic issues, these setups are still difficult to align for small F-numbers and are therefore usually large in size as well.

In a previous work[18], we showed that telescopes based on off-axis parabolic mirrors (OAPs) represent a reliable and attractive solution for large-aperture systems as long as a suitable alignment setup is employed. As these optics are commercially available with small F-numbers and can, in principle, compose aberration-free telescopes, an OAP telescope is a viable solution for compact beam transport. In addition, the use of an OAP enables implementing a true equivalent-target-plane imaging strategy, as OAPs are in general also used as the last focusing system of a high-energy short-pulse laser.

In this work, we describe the design of the ultra-compact imaging WF sensor, the so-called petawatt target area sensor (PTAS), that is now installed after the pulse compressor of the Petawatt High-Energy Laser for heavy Ione Xperiments (PHELIX) facility at the GSI Helmholtzzentrum für Schwerionenforschung in Darmstadt, Germany.

Firstly, we list the dimensioning requirements for the PTAS in Section 2 and derive a suitable setup, using findings from our previous work. In Section 3, we describe the technical realization of the PTAS in detail. For the optimization of the focal spot, we performed some initial tests of a calibration scheme for the PTAS, which we describe in Section 4. In order to prove this concept, we show experimental results supporting the claim of increased on-shot intensity in Section 5. Finally, we summarize our results in Section 6, showing that we succeeded to increase the peak intensity at PHELIX by a factor of three using a full post-compressor, ultra-compact AO loop. This enables reaching intensities beyond 10^{21} W/cm^2 at PHELIX.

2. Design requirements

The goal of this work was to design and implement all the components of a post-compressor AO system at PHELIX. These components include the DM as the active component, the beam sensor PTAS and a calibration device, which is able to provide an absolute reference for the WF inside the target chamber.

We purchased a DM from ISP System, France, which features an aperture large enough to take the 28 cm beam at an angle of incidence of 45°, and placed it at the exit of the compressor area (Figure 1). In the following, we will

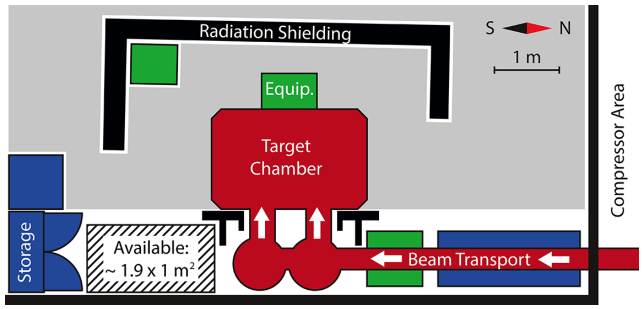

Figure 1. Scale sketch of the PHELIX target area before the installation of the PTAS. The DM will be placed in the compressor area to the right, while the available space for the PTAS is indicated by the ruled area on the left. The light gray region indicates the area reserved for user equipment and personnel access.

cover the design considerations of the PTAS, while we will describe the calibration device in Section 4.

The requirements for the design of the PTAS can be split into two parts: those driven by the application and those driven by the site itself. The latter is defined by the space constraints close to the target chamber at PHELIX. Given the close proximity of the compressor tank to the chamber, only one place is suitable for the PTAS. Here, an area of only roughly 2 m^2 is available (see Figure 1), which means that the complete system, including the demagnification of the beam, has to be designed accordingly.

The application sets different requirements, as follows.

(1) *Bandwidth*: the pulses at PHELIX feature a bandwidth of approximately 5 nm, centered around a WL of 1053 nm. The setup should be achromatic in this range.

(2) *Beam demagnification*: the full aperture of the incoming beam can be as large as 280 mm in diameter and has to be resized to a maximum of 5 mm. This means the demagnification factor has to be at a minimum of 56.

(3) *Imaging of the DM*: for the AO loop to work correctly, the surface of the DM has to be imaged onto the WF sensor.

(4) *High dynamic range*: as PHELIX is only able to shoot every 90 minutes, the control loop has to run in alignment mode, pre-compensating for the aberrations of the shot. Using the same setup, the on-shot WF shall be measured, which means the PTAS has to be able to cope with a dynamic range of about 5×10^5 and everything in between continuously.

(5) *Appropriate transmitted WF*: the PTAS is not intended to provide an absolute WF measurement, as a calibration routine shall be employed. However, a good accuracy is still desirable to allow easier estimation of the performance of the laser system. Given that a Strehl ratio of 0.9 is acceptable, this corresponds to

an approximate root mean square (RMS) WF error of 0.052λ[19] (for pure astigmatism in the Zernike sense, this equals 0.286λ PtV). At PHELIX, the central wavelength is 1053 nm.

As stated above, the demagnification of the beam cannot be done with conventional refractive optics, due to the combination of the large diameter and short pulse duration. Instead, an OAP telescope can be used.

The standard focusing optic for experiments at PHELIX is a 45°, $f = 400$ mm OAP. Focusing a beam with a diameter of up to 280 mm and using a corresponding OAP to recollimate the light afterwards makes a very short telescope. However, the small F-number indicates high sensitivity to alignment errors, which has to be investigated.

In a previous work[18], we presented an alignment scheme for OAP telescopes, based on the overlap of the focal spots of both OAPs using a back-propagating alignment beam. In the same work, we delivered straightforward estimation formulae for the alignment precision that can be expected and the WF defects that would be caused by the errors. With an F-number of 1.43 and an off-axis angle of 45°, these estimations yield a maximum WF error of $\Delta_{\text{trans}} = 0.0184\,\lambda$ RMS for transversal misalignment and $\Delta_{\text{long}} = 0.0518\lambda$ RMS for longitudinal misalignment.

As we stated above in the list of requirements, the RMS of the transmitted WF should be below 0.052λ. Obviously, the maximum transversal WF error, which primarily consists of astigmatism and coma[18], easily fulfills this requirement. The maximum longitudinal error, on the other hand, stresses the given limit. However, the associated WF deviation in this case mainly consists of defocusing, which can easily be compensated for by the following telescopes.

3. Technical realization

In this section, we describe the technical realization of the PTAS in detail.

3.1. Overview

Figure 2 shows a schematic of the PTAS and is true to scale. The beam entering from the right is the leakage light of the last turning mirror (transmission = 0.5%) of the main beam. We estimated the B-integral in the bulk material of the mirror for a pulse of 200 J and 500 fs duration using an image of the NF (see Figure 3). The result was (0.261 ± 0.075) radians in the mean, peaking at 0.555 radians. This is still within tolerable limits.

At this point, the main beam features a diameter of up to 280 mm, depending on the selected aperture. The main demagnification happens using a compact 8:1 OAP telescope, described in Section 3.2, while still being in vacuum, as the intensity at the intermediate focal spot would be

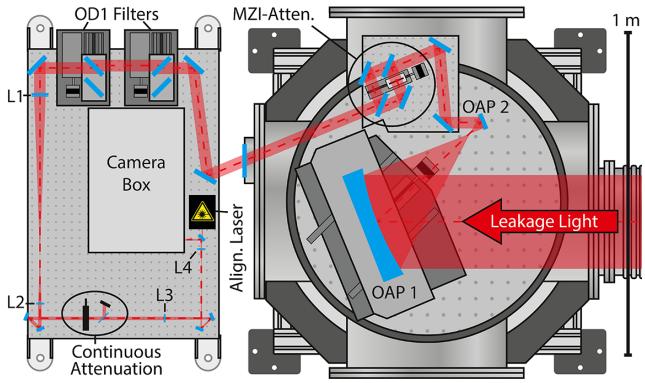

Figure 2. Scale schematic of the PTAS. The intermediate focal diagnostic is not shown for clarity. The other main components are labeled ('L' for lenses) and described in the text.

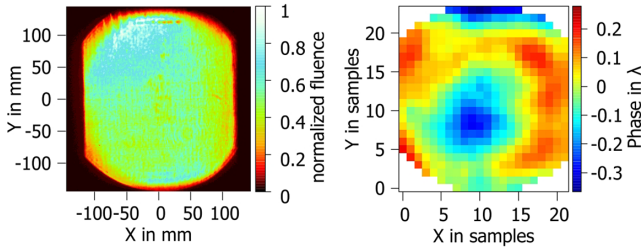

Figure 3. The NF (left) and absolute, uncorrected WF (right) at the PTAS, recorded on-shot using the largest possible aperture.

sufficient to ionize gas. The alignment is done with an intermediate focal diagnostic (not shown in Figure 2), which is described in Section 3.4.

The energy is optionally attenuated with another leaky mirror, where the beam paths are overlapped using a Mach–Zehnder style configuration and a shutter to select the beam path, described in Section 3.3. At this point, the energy is already low enough to make the contribution to the overall B-integral in the material of the leaky mirror insignificant.

Afterwards, the beam leaves the vacuum chamber and passes two motorized, reflective neutral density filters for further energy attenuation, which is standard at PHELIX. The beam is then further demagnified about a factor of 3.3 by a regular Kepler telescope, composed of achromats. It passes through a continuously variable attenuator, using a $\lambda/2$ waveplate and polarizer combination, and another achromatic Kepler telescope, which applies final demagnification by a factor of 2.4 and images the DM into a camera box, featuring both NF and far field (FF) cameras and a custom Shack–Hartmann sensor (SHS) for WF measurement.

3.2. Demagnification and imaging

The decision to demagnify the beam using an OAP telescope follows from the requirement of compactness, while the decision for an $f_1 = 400$ mm, 45° OAP as the first

optical element was made due to compliance with PHELIX standards.

For the second OAP, the main aspects considered were its damage threshold and producibility. As 0.5% of the main beam is transmitted through the leakage mirror towards the PTAS, a hypothetical demagnification of 14:1 would yield the same NF fluence in the main beam, which we consider the limit in order to avoid the risk of damage.

On the other hand, an OAP equivalent to the first one but a factor of 14 smaller is very difficult to produce due to the strong curvature of the substrate. After a comprehensive survey, we found that a focal length of $f_2 = 50$ mm seemed to be an acceptable trade-off between size and accuracy. Furthermore, the beam diameter of 35 mm after the telescope is still large enough to slow down the formation of hot spots until the beam has been attenuated. We also chose coatings that could tolerate any conceivable fluctuations in local intensity up to that point.

Our OAP was milled from a 2" copper substrate (LT Ultra GmbH, Germany), featuring a surface error of less than 150 nm peak-to-valley (PtV) and a roughness of less than 5 nm RMS. This is still relatively large and shows that the estimated alignment errors are not the limiting factor for the transmission beam quality of the PTAS.

Thanks to the smaller beam diameter after the OAP telescope, the rest of the imaging and demagnification can be done with off-the-shelf achromats, given that the energy is sufficiently attenuated before, as even large F-number telescopes will not stress the space constraints. The second telescope is composed of one $f = 500$ mm and one $f = 150$ mm achromatic doublet (labeled 'L1' and 'L2' in Figure 2). The third telescope brings the beam diameter down to 4.4 mm using one $f = 300$ mm and one $f = 125$ mm achromatic doublet (labeled 'L3' and 'L4' in Figure 2, respectively) and images the surface of the DM onto the image plane of the camera box. The chromatic defocusing over the full width at half maximum (FWHM) of the PHELIX spectrum introduced by these lenses is less than 0.01λ RMS, which is better than the alignment precision of the OAP telescope.

In Figure 3, the NF and WF at the PTAS are shown. These were recorded on-shot using the largest possible aperture at PHELIX. In the NF, the clipping of the beam on the last compressor grating (see Section 5.1) is visible on the left- and right-hand side of the beam, together with grating imperfections at various places in the NF. This demonstrates the NF imaging quality of the PTAS. The according WF shows that high-order aberrations dominate the beam, while astigmatism and defocusing are mostly absent.

3.3. Energy attenuation

The range of available energies in the target chamber of PHELIX goes from 400 μJ for the alignment beam to 200 J for a full energy shot, while most energies in between can also be achieved. The dynamic range that has to be covered by the PTAS is therefore 5×10^5, which has to be achieved with several attenuation stages.

The first attenuator is a Mach–Zehnder setup right after the OAP telescope (labeled 'MZI-Atten.' in Figure 2). Here, the first beam splitter is a leaky mirror with a reflectivity of 99.3%, while the recombination beam splitter has a reflectivity of 40% (for s-polarization, as present in the PTAS). A motorized shutter can block either one or the other beam path, enabling the selection between transmissions of 59.58% and 0.28%, respectively, creating a dynamic range of 2.13×10^2.

Outside of the vacuum chamber, before the beam gets further demagnified, two reflective attenuators with a neutral density of 1 can be inserted into the beam, increasing the dynamic range to 2.13×10^4.

The rest of the dynamic range is given by the last attenuator, which is a combination of a $\lambda/2$ wave plate and a single polarizer and is easily capable of attenuating the energy by the required factor of 24.

In order to avoid ghost images, we applied standard measures to this setup. Specifically, all planar optics except the neutral density filters are wedged and the ghost images are removed from the beam path by a pinhole in the intermediate focal plane between L1 and L2. The neutral filters, however, feature plane-parallel surfaces, as the beam displacement introduced by the first filter has to be compensated by the second one. Here, an anti-reflective coating with a reflectivity of less than 0.2% mitigates ghost images to an insignificant amount.

With most of the coatings being susceptible to polarization, the PTAS proved to handle linear polarization well, achieving the desired extinction ratio at any pulse energy that can be delivered by PHELIX and thus being able to measure over the whole energy range.

3.4. Alignment strategy

The alignment of the beam path outside of the vacuum chamber was done using a back-propagating reference beam, generated by a fiber laser, which was injected next to the camera box (see Figure 2). Using a 0° turning mirror after the second telescope, it was used in a double-pass configuration to optimize the alignment with the WF sensor of the camera box.

However, the alignment beam stayed in place afterwards for the alignment of the OAP telescope, using the alignment scheme described in our previous work[18], where the intermediate focal spots of the main beam and the back-propagating alignment beam were overlapped spatially.

In order to do so, an etched tungsten needle on a motorized stage is used to mark the position of the focal spot (see

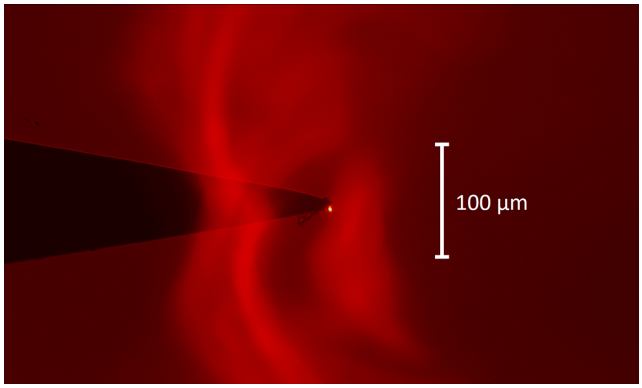

Figure 4. An etched tungsten needle is used to mark the position of the focal spot (center). A bit of dust has stuck on its tip. The large caustics are created by backlighting, which is used in order to see the shadow of the needle.

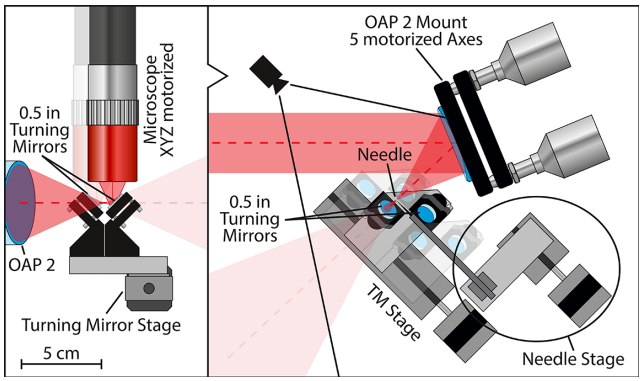

Figure 5. Scale schematic of the intermediate focal diagnostic in side view (left) and top view (right), observing the backwards propagating alignment beam. The needle and the diagnostic mirrors can be moved in and out of the beam, while the microscope can be moved in three axes in order to change the viewing position. The other possible states of the diagnostic are drawn as transparent overlays.

Figure 4). The focal plane then has to be observed in both beam directions with a vacuum compatible microscope that is able to resolve the intermediate focal spot. Due to the small focal length of the second OAP, this setup has to be rather compact in this case, generating the necessity of two small mirrors that can be placed in the beam after the focal spot for each propagation direction, respectively (see Figure 5) in order to deflect the beam into the microscope.

Our microscope is composed of a 20× Plan Apo NIR infinity-corrected objective (Mitutoyo Corp., Japan) combined with an $f = 200$ mm plano-convex lens and a 12-bit CMOS camera (Manta G-235B, Allied Vision Technologies GmbH, Germany). Cooling the camera under vacuum is significantly simplified by the fact that this board-level camera is split into a sensor and a connector board, connected by a flexible flat cable. As most of the heat is only generated on the connector board, it can easily be mounted to a dedicated heat sink.

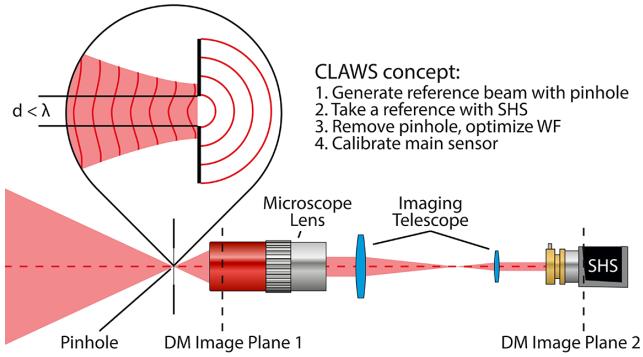

Figure 6. Schematic of the CLAWS concept.

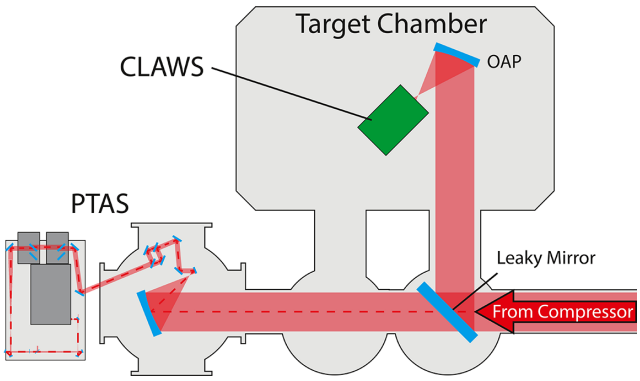

Figure 7. Sketch of the target chamber area, indicating a possible configuration during the calibration routine.

4. Calibration

The quality of the detector is defined by its ability to deliver a focal spot representation as close to reality as possible. This task is not easy, as the on-shot intensity distribution in the target chamber is usually not accessible. Therefore, a cross-calibration procedure, performed at low intensity, was developed.

4.1. Cross calibration

As mentioned earlier, the optimization of the focal spot requires a calibration routine for the WF sensor. As the PTAS inherently measures the leakage of the beam, the calibration has to be done separately, sampling the actual focused beam.

To do so, we developed a module named Calibrator for Laser systems with Absolute Wavefront Sensing (CLAWS). This module is depicted schematically in Figure 6. The strength of CLAWS lies in its ability to be self-calibrated *in situ* using a pinhole[20–22] in the focal plane, creating a spherical WF as reference. In addition, the system is compact and can be moved to the target chamber center (see Figure 7) at the beginning of the experiment to cross-calibrate the PTAS with the least amount of interference with the experimental setup.

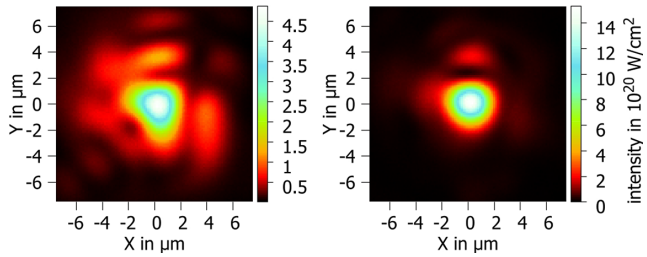

Figure 8. The unoptimized (left) and optimized (right) focal spots of a copper OAP at the target position, recorded with a 16-bit CMOS camera, installed in CLAWS. The intensity is estimated for a 100 J, 500 fs pulse.

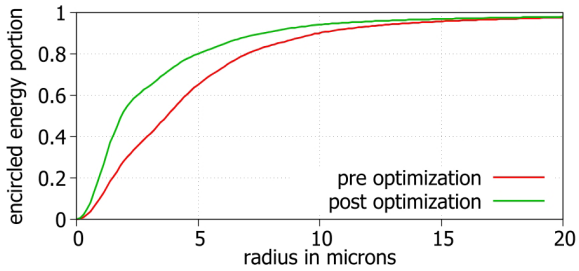

Figure 9. The encircled energy over the radius from the point of largest intensity, taken for the focuses shown in Figure 8.

In practice, CLAWS is aligned to catch the full beam with a high-numerical-aperture microscope objective. Then, a (1+0.25/–0.10) µm blackened stainless steel foil pinhole, manufactured by Thorlabs Inc., USA, is placed in the focus to generate a close-to-perfect spherical wave. Using this ideal point source, a reference is taken using CLAWS. Afterwards, the pinhole is removed and the AO runs an optimization loop to this reference (see next section for results). Once the best WF is reached, the WF measured by the PTAS is saved as the new PTAS WF reference, corresponding to the best accessible focus at the target position. After this procedure, CLAWS can be removed.

4.2. *Optimization results*

The focal spot before and after the optimization using CLAWS is shown in Figure 8. After we completed the calibration routine for the first time, the peak fluence in the focal plane increased by roughly a factor of three, promising more than 10^{21} W/cm^2 for a typical PHELIX shot of 100 J and 500 fs. The improvement is obvious, as most of the scattered energy is moved back into the center of the focal spot. This becomes especially apparent when looking at the encircled energy, shown in Figure 9, as the curve of the optimized focal spot lies consistently above the unoptimized one. The radius of 50% encircled energy, for example, is only half as large as prior to the optimization.

The WFs in CLAWS, associated with these focuses, are shown in Figure 10. The remaining high-order aberrations, relative to the pinhole reference, are visible on the right.

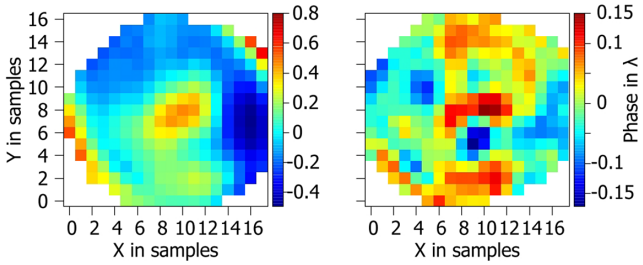

Figure 10. The unoptimized (left) and optimized (right) WFs corresponding to the focuses shown in Figure 8, recorded using CLAWS. The WFs are measured relative to the reference generated using the pinhole. The unoptimized WF features an RMS of 0.202λ, while it is reduced to 0.052λ after optimization.

These aberrations, combined with steep slopes at the edges of the beam and some yet uncharacterized chromatic aberrations that cannot be corrected using a DM, are accountable for the deviations of the optimized focal spot from the diffraction limit.

By now, CLAWS can only be operated in air, which leads to some uncertainty in the estimation of the on-shot intensity after the target chamber has been evacuated. Doing quantified measurements of the associated alignment deviations of the focusing OAP relative to the incoming beam, we found these uncertainties to yield a correction factor of $0.84^{+0.16}_{-0.03}$, which we applied to all findings presented in the following.

5. Experimental validation

5.1. *Image quality of the PTAS*

While the PTAS does not need to deliver a true FF intensity distribution representation of the beam due to the calibration procedure using CLAWS, it was designed to allow a high-fidelity low-distortion imaging of the sampled beam to the detectors. To check this point, we needed to compare the FF at the PTAS with a reference. The focal spot in the target chamber is, however, not suitable for this, as the OAPs are changed and realigned between experiments, drastically changing the aberrations in the chamber. Therefore, we compared FF images recorded at the PTAS with images recorded at the compressor beam sensor, which uses a high-F-number ($f = 6$ m) lens as the first optic for imaging (see Figure 11). Figure 12 shows a snapshot of the FF here (left) and at the PTAS (right). The images were recorded at the same time and without any beam correction.

The focal fluence distributions show obvious qualitative similarities, while deviations indicate some difference between the beam paths. This is presumably composed of astigmatism and defocusing, but cannot be quantified due to the lack of a WF sensor at the compressor exit sensor. Still, the similarity shows that the PTAS can be used as a sensor calibrated to a relative reference, while at the same time

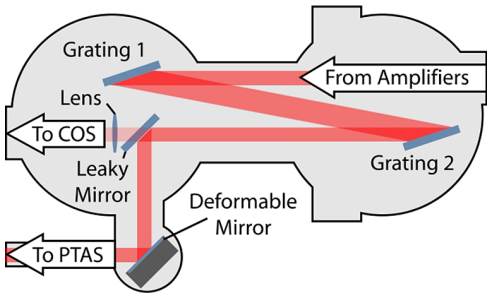

Figure 11. A sketch of the PHELIX compressor, including the gratings, the DM and the directions to the compressor beam sensor ('COS') and the PTAS.

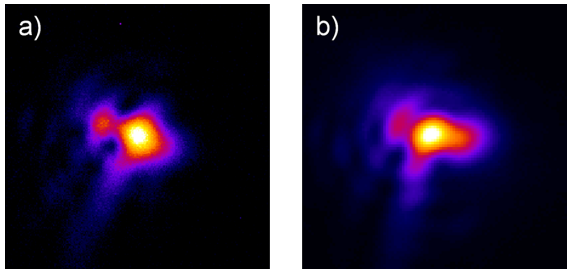

Figure 12. A qualitative comparison between FFs (a) measured at the compressor exit and (b) measured at the PTAS at the same time. No beam correction was applied.

aiding the laser operation by providing an approximation of the FF at the target position.

The statement that these deviations are not the limiting factor in the FF approximation holds especially true when considering the difference between the uncorrected FF recorded at the compressor and the PTAS (Figure 12) and the uncorrected FF at the target position (Figure 8, left). This difference is due to the aberrations introduced by the imperfections of the focusing optic (in this case, an OAP milled from copper). It will persist even if the focal spot is optimized and change if the focusing optic is replaced.

5.2. *On-shot intensity gain*

Finally, we conducted an experiment to verify the increase in on-target intensity. During this campaign, we investigated the impact of the higher intensity on the laser–target interaction. Specifically, we used the PTAS and the AO loop to control and estimate the on-shot intensity for the different configurations described below while keeping the pulse energy constant and varying the thickness of the foil targets made of polystyrene.

Under our experimental conditions, a higher laser intensity increases the hole-boring effect[23]. Therefore, we expect the transmission of the laser light through the target to depend on the target thickness and the intensity reached on-shot, where lower thicknesses and higher intensities increase the transmission. The results of this measurement are shown in

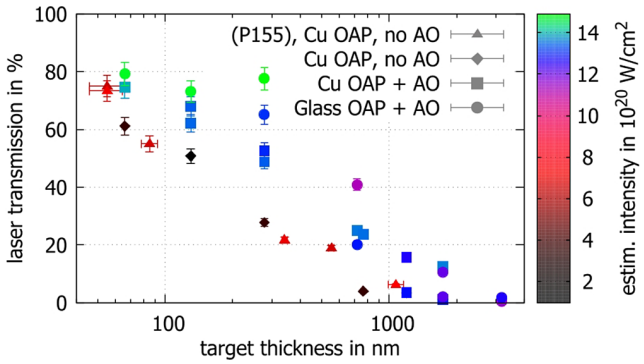

Figure 13. Transparency of the polystyrene foil targets, plotted over their thickness. The estimated intensities are color coded, while different shot configurations are indicated by the shape of the data points. The data set displayed as triangles was taken from a previous beam time (P155).

Figure 13, plotting the transmission through the target over the foil thickness in the range from (55 ± 9) nm to (3186 ± 15) nm for various operation conditions.

Due to the Treacy architecture[24] of the PHELIX compressor (see Figure 11), the pulse is spatially chirped when entering the target chamber and the PTAS. This leads to some ambiguity in the data of the SHS and makes calculating the exact fluence distribution in the target plane a complicated task. Therefore, we estimated the intensity by viewing the focal spot with a 16-bit CMOS camera after the calibration routine, applying the expected error arising from the pump-down, as discussed in Section 4. We then used the on-shot deviation of the WF at the PTAS compared to the calibration reference to derive a multiplicative factor (Strehl) for this intensity. The result is color coded in Figure 13. Note that the choice of using a color bar for the intensity prevents us from showing the error of the intensity, which is within +28% to −18% and contributes to the scattering of the data points along the *y*-axis.

The diamonds and triangles correspond to two different experiments without AO, yielding similar results and intensities of about $(1.4–3.6)\times10^{20}$ W/cm^2. Using the AO loop in combination with the copper parabola increases the on-target intensity by a factor of three to five (squares), while using a glass parabola increases the intensity even more up to 1.4×10^{21} W/cm^2 (green dots). This indicates that the AO loop cannot fully correct for the high spatial frequency defects that are present on a milled copper OAP, pointing out the advantages of polished glass OAPs.

While one expects a transmission of 100% in the limit of an infinitely thin target, we only reach about 80% in this experiment, where the shots using the glass OAP may indicate some form of saturation. This can be explained by the lower intensity parts of the focal spot, which do not contribute to the hole boring and are rather reflected by the plasma. However, we could not investigate this as no targets thinner than 55 nm were available.

A clear correlation between intensity and transmission through the target is apparent, where the target becomes transparent at smaller thicknesses and for higher intensities, which matches our expectations. The greatest impact of the intensity is visible at target thicknesses around 300 nm, increasing the transmission from about 30% to 65% using a copper OAP with AO and almost 80% if a glass OAP was used instead. This shows the robustness of the WF sensing and the AO loop.

Note that the shots with the glass OAP for target thicknesses over 500 nm are of lower intensity. These were the first shots with AO, where the shot routine still needed to be debugged. Due to time constraints, these shots could not be repeated.

6. Summary and outlook

In this work, we described the concept and implementation of a novel, ultra-compact post-compressor WF sensor design for the PHELIX laser system, called the PTAS. The key component is a compact demagnification system composed of an $F = 1.43$ OAP telescope, which is aligned using an intermediate focal diagnostic. It has been shown that this alignment strategy yields sufficient precision to estimate the shape of the focal spot on target.

We also presented a calibration strategy for the PTAS, which involves a mobile WF sensor (CLAWS) behind the target location to optimize the focal spot at the target position. CLAWS itself uses a diffraction-limited spherical wave as reference, which is generated in the focal plane by a small pinhole. Using real data, we estimated an intensity gain by a factor of three that can be expected on-shot using AO. In addition, we demonstrated this during an experimental campaign, observing the laser transmission through foil targets, where higher estimated intensity consistently matched higher transmission through the target. For full energy shots, intensities of 10^{21} W/cm^2 can now be reached systematically at PHELIX. This was only possible using the on-shot diagnostic capabilities of the PTAS.

While we provided a proof of principle, further work has to be done to implement this strategy into the daily operation of PHELIX. Primarily, the evacuation process of the whole vacuum complex introduces deformations to the optical breadboards that are difficult to measure and lead to loss of the calibration references. We estimated the associated factor of the intensity, including uncertainty, to be $0.84^{+0.16}_{-0.03}$, which means that up to 16% of intensity could be gained by engineering CLAWS to operate in vacuum and thus calibrate the PTAS to the actual shot conditions in the chamber.

After this is done, the new focus optimization loop can be used in community experiments.

Acknowledgments

The authors thank Treofan Germany GmbH & Co. KG for kindly providing polypropylene foils with a thickness of 1.9 μm for the experimental campaigns.

This work has received partial funding from the EUROfusion Consortium, funded by the European Union via the Euratom Research and Training Programme (Grant Agreement No. 101052200—EUROfusion).

References

1. C. N. Danson, C. Haefner, J. Bromage, T. Butcher, J.-C. F. Chanteloup, E. A. Chowdhury, A. Galvanauskas, L. A. Gizzi, J. Hein, D. I. Hillier, N. W. Hopps, Y. Kato, E. A. Khazanov, R. Kodama, G. Korn, R. Li, Y. Li, J. Limpert, J. Ma, C. H. Nam, D. Neely, D. Papadopoulos, R. R. Penman, L. Qian, J. J. Rocca, A. A. Shaykin, C. W. Siders, C. Spindloe, S. Szatmári, R. M. G. M. Trines, J. Zhu, P. Zhu, and J. D. Zuegel, High Power Laser Sci. Eng. **7**, e54 (2019).
2. W. P. Leemans, A. J. Gonsalves, H.-S. Mao, K. Nakamura, C. Benedetti, C. B. Schroeder, C. Tóth, J. Daniels, D. E. Mittelberger, S. S. Bulanov, J.-L. Vay, C. G. R. Geddes, and E. Esarey, Phys. Rev. Lett. **113**, 245002 (2014).
3. J.-P. Zou and B. Wattellier, in *Topics in Adaptive Optics* (Intech, 2012), Chapter 5.
4. N. Lefaudeux, X. Levecq, G. Dovillaire, S. Theis, and L. Escolano, Proc. SPIE **8236**, 82360K (2012).
5. C. N. Danson, P. A. Brummitt, R. J. Clarke, J. L. Collier, B. Fell, A. J. Frackiewicz, S. Hancock, S. Hawkes, C. Hernandez-Gomez, P. Holligan, M. H. R. Hutchinson, A. Kidd, W. J. Lester, I. Musgrave, D. Neely, D. R. Neville, P. A. Norreys, D. Pepler, C. J. Reason, and B. E. Wyborn, Nucl. Fusion **44**, S239 (2004).
6. P. Mckenna, S. P. D. Mangles, G. Sarri, and J. Schreiber, Rom. Rep. Phys. **68**, S145 (2016).
7. J. W. Yoon, Y. G. Kim, I. W. Choi, J. H. Sung, H. W. Lee, S. K. Lee, and C. H. Nam, Optica **8**, 630 (2021).
8. J. M. Soures, R. J. Hutchison, S. D. Jacobs, L. D. Lund, R. L. McCrory, and M. C. Richardson, in *Symposium on Fusion Engineering* (1983), p. 1.
9. J. Bromage, S.-W. Bahk, D. Irwin, J. Kwiatkowski, A. Pruyne, M. Millecchia, M. Moore, and J. D. Zuegel, Opt. Express **16**, 16561 (2008).
10. D. N. Papadopoulos, J. P. Zou, C. Le Blanc, G. Chériaux, P. Georges, F. Druon, G. Mennerat, P. Ramirez, L. Martin, A. Fréneaux, A. Beluze, N. Lebas, P. Monot, F. Mathieu, and P. Audebert, High Power Laser Sci. Eng. **4**, e34 (2016).
11. J. P. Zou, C. Le Blanc, D. N. Papadopoulos, G. Chériaux, P. Georges, G. Mennerat, F. Druon, L. Lecherbourg, A. Pellegrina, P. Ramirez, F. Giambruno, A. Fréneaux, F. Leconte, D. Badarau, J. M. Boudenne, D. Fournet, T. Valloton, J. L. Paillard, J. L. Veray, M. Pina, P. Monot, J. P. Chambaret, P. Martin, F. Mathieu, P. Audebert, and F. Amiranoff, High Power Laser Sci. Eng. **3**, e2 (2015).
12. N. Blanchot, G. Béhar, J. C. Chapuis, C. Chappuis, S. Chardavoine, J. F. Charrier, H. Coïc, C. Damiens-Dupont, J. Duthu, P. Garcia, J. P. Goossens, F. Granet, C. Grosset-Grange, P. Guerin, B. Hebrard, L. Hilsz, L. Lamaignere, T. Lacombe, E. Lavastre, T. Longhi, J. Luce, F. Macias, M. Mangeant, E. Mazataud, B. Minou, T. Morgaint, S. Noailles, J. Neauport, P. Patelli, E. Perrot-Minnot, C. Present, B. Remy, C. Rouyer, N. Santacreu, M. Sozet, D. Valla, and F. Laniesse, Opt. Express **25**, 16957 (2017).

13. M. Hornung, H. Liebetrau, S. Keppler, A. Kessler, M. Hellwing, F. Schorcht, G. A. Becker, M. Reuter, J. Polz, J. Körner, J. Hein, and M. C. Kaluza, Opt. Lett. **41**, 5413 (2016).
14. J. Bromage, S.-W. Bahk, I. A. Begishev, C. Dorrer, M. J. Guardalben, B. N. Hoffman, J. B. Oliver, R. G. Roides, E. M. Schiesser, M. J. Shoup, M. Spilatro, B. Webb, D. Weiner, and J. D. Zuegel, High Power Laser Sci. Eng. **7**, e4 (2019).
15. J. Néauport, N. Blanchot, C. Rouyer, and C. Sauteret, Appl. Opt. **46**, 1568 (2007).
16. S.-W. Bahk, J. Bromage, and J. D. Zuegel, Opt. Lett. **39**, 1081 (2014).
17. E. M. Schiesser, S.-W. Bahk, J. Bromage, and J. P. Rolland, Appl. Opt. **58**, 9514 (2019).
18. J. B. Ohland, Y. Zobus, U. Eisenbarth, B. Zielbauer, D. Reemts, and V. Bagnoud, Opt. Express **29**, 34378 (2021).
19. V. N. Mahajan, J. Opt. Soc. Am. **73**, 860 (1983).
20. D. Wang, F. Wang, H. Zou, and B. Zhang, Appl. Opt. **52**, 7602 (2013).
21. G. Ding, Y. Qi, Z. Lu, and G. Liu, Proc. SPIE **9282**, 92821U (2014).
22. F. Gao, Z.-F. Jiang, and B. Li, Proc. SPIE **7656**, 76565Y (2010).
23. J. Hornung, Y. Zobus, S. Roeder, A. Kleinschmidt, D. Bertini, M. Zepf, and V. Bagnoud, Nat. Commun. **12**, 6999 (2021).
24. E. Treacy, IEEE J. Quantum Electron. **5**, 454 (1969).